

Learning Local Distribution for Extremely Efficient Single-Image Super-Resolution

Wei Wu, Wen Xu, Bolun Zheng *, Aiai Huang and Chenggang Yan

School of Automation, Hangzhou Dianzi University, Hangzhou 310018, China; ww@hdu.edu.cn (W.W.); 212050284@hdu.edu.cn (W.X.); huangaiai@hdu.edu.cn (A.H.); cgyan@hdu.edu.cn (C.Y.)

* Correspondence: blzheng@hdu.edu.cn

Abstract: Achieving balance between efficiency and performance is a key problem for convolution neural network (CNN)-based single-image super-resolution (SISR) algorithms. Existing methods tend to directly output high-resolution (HR) pixels or residuals to reconstruct the HR image and focus a lot of attention on designing powerful CNN backbones. However, this reconstruction way requires the CNN backbone to have good ability to fit the mapping function from LR pixels to HR pixels, which certainly held these methods back from achieving extreme efficiency and from working in embedded environments. In this work, we propose a novel distribution learning architecture to estimate the local distribution and reconstruct HR pixels by sampling the local distribution with the corresponding 2D coordinates. We also improve the backbone structure to better support the proposed distribution learning architecture. The experimental results demonstrate that the proposed method achieves state-of-the-art performance for extremely efficient SISR and exhibits a good balance between efficiency and performance.

Keywords: image super-resolution; local distribution model; extreme efficient; multi-layer neural network



Citation: Wu, W.; Xu, W.; Zheng, B.; Huang, A.; Yan, C. Learning Local Distribution for Extremely Efficient Single-Image Super-Resolution. *Electronics* **2022**, *11*, 1348. <https://doi.org/10.3390/electronics11091348>

Academic Editor: Andrea Prati

Received: 12 March 2022

Accepted: 19 April 2022

Published: 24 April 2022

Publisher's Note: MDPI stays neutral with regard to jurisdictional claims in published maps and institutional affiliations.



Copyright: © 2022 by the authors. Licensee MDPI, Basel, Switzerland. This article is an open access article distributed under the terms and conditions of the Creative Commons Attribution (CC BY) license (<https://creativecommons.org/licenses/by/4.0/>).

1. Introduction

Single image super-resolution (SISR) is a classic image processing task, which has been catching researchers' attention for decades. The SISR targets reconstructing a high-resolution (HR) image with only one low-resolution (LR) image as input. Reconstructing clear and accurate edges is one of the major challenges in SISR.

Early studies focus on interpolation-based algorithms [1–3] that aim to calculate the sub-pixels with neighboring pixels. Due to the limited information on the neighboring pixels, interpolation-based methods fail to reconstruct visually clear edges. Introducing filtering-based methods for post-processing to enhance the interpolated image is another option [4,5]. These methods introduce non-local information [6] and non-linear filtering and certainly enhance the visual quality of the interpolated image. However, limited by the fronted interpolation methods, they also struggle to handle the large upsampling factors. The optimization-based methods introduce kinds of priors and approach the optimal results in an iterative way [7,8]. Limited by the complicated iterative solutions, these methods are usually quite inefficient. Moreover, because the statistical priors cannot fit all samples, the optimization-based methods also suffer from poor robustness. With the development of machine learning, lots of data-driven methods have been proposed [9–11]. The sparse coding-based methods [12–14] introduce a learning-based encoder to sparsely encode both LR patches and HR patches and then try to build the mapping function from LR patches to HR patches with sparse representation. However, the separated learning strategy and limited sparse representation certainly limit the performance of these methods.

Benefiting from the great growth of computation devices, deep-learning-based methods exhibit a promising performance, and some of them widely are adopted in the edge devices, such as surveillance cameras and mobile phones. Due to the power limitation

and computational resource limitation, the efficiency is always firstly considered when deploying the algorithms to such edge devices.

Dong et al. [11] introduced a convolution neural network [15] and provided an end-to-end learning architecture named SRCNN for the SISR task. They first use bi-cubic interpolation to upsample the LR image to the target resolution and then introduce CNN to reconstruct the HR image from the upsampled LR image. In this situation, the CNN has to work on the upsampled images, which extends the time of calculation and is quite inefficient. Several studies [16,17] introduce transpose convolution [18] to conduct the upsampling operation within the CNN architecture. Some studies try to implement bilinear interpolation within the CNN architecture to directly upsample the convolution feature map using bilinear interpolation. Due to the limited upsampling accuracy, these two operations could only work in the middle of the network. Therefore, parts of the convolution layers also have to work on the upsampled resolution. To overcome this limitation, Shi et al. [19] introduce a pixel shuffle operation and propose a sub-pixel learning network named ESPCN for SISR. Unlike previous studies that directly output the reconstructed HR image, ESPCN outputs the sub-pixels at each position and shuffle the sub-pixels to obtain the final HR image. By doing so, the upsampling operation is moved to the end of the network, so that the whole CNN could work on the original resolution.

Then, lots of studies adopted the pixel shuffle operation to reconstruct the HR pixels and focus on the powerful and efficient backbone to achieve a balance between performance and efficiency. Increasing the depth and introducing more components are general ways to obtain more powerful backbones [20,21]. Introducing and optimizing the residual-like components are widely adopted in relative research [22,23]. Liu et al. [24] propose a residual feature aggregation (RFA) framework to aggregate these informative residual features to produce more representative features. Zhang et al. [25] propose a context reasoning attention network (CRAN) to adaptively modulate the convolution kernel according to the global context for the SISR task. Zhang et al. [26] propose an end-to-end trainable unfolding network that leverages both learning-based methods and model-based methods. The network inherits the flexibility of model-based methods while maintaining the advantages of learning-based methods. Other studies [27,28] introduce a Generative Adversarial Network (GAN) to process real-world LR images, which are do not perform well based on CNN methods.

Though these methods could significantly improve the performance, they are hardly deployed on hardware platforms [29,30] because of the extreme efficiency requirement. In this paper, we rethink the SISR task along the signal sampling direction and propose a CNN-based local distribution reconstruction network (LDRN) for an extremely efficient SISR task, aiming to provide a new baseline for hardware platforms.

The LDRN first introduces a neural network model to reconstruct the distribution of the neighbor area of each LR pixel and then calculates the sub-pixels within the neighboring area based on their relative coordinates from the center pixel. Compared to existing methods, the proposed method achieves an excellent balance in efficiency and performance, exhibiting good potential for being deployed to hardware platforms.

2. Proposed Method

Given a scene and a camera lens, the resolution of the captured image depends on the number of photosensitive cells on the image sensor. Increasing the density of the photosensitive cells is a direct way to increase the resolution of the captured image. Assuming the real signal distribution of the scene is \mathbf{D} , the sampling matrix of the image sensor is \mathbf{M} , and the captured image I can be expressed as:

$$I = S(\mathbf{D}, \mathbf{M}), \quad (1)$$

where S denotes a sampling function. Therefore, changing the sampling matrix \mathbf{M} directly affects the resolution of the captured image. Because \mathbf{M} is always uniformly arranged, the corresponding sampling matrix of an HR image \mathbf{M}_{HR} can be easily calculated. Therefore,

the keypoint of calculating the HR image from an LR image is reconstructing the scene's distribution \mathbf{D} .

2.1. Motivation

A static natural scene is a 3D signal. After the optic transformation is conducted by the camera lens, the scene's signal degrades to a 2D signal $\mathcal{S}(x, y)$ lying on the image plane. Because the $\mathcal{S}(x, y)$ totally depends on the scene, it is hard to give a specific mathematical model to describe the $\mathcal{S}(x, y)$. We try to decompose the $\mathcal{S}(x, y)$ into multiple patches and reconstruct the local distribution of each patch for sub-pixel reconstruction.

Because all observed pixels are uniformly arranged, we set the horizontal (or vertical) distance between two adjacent pixels in the LR image as the unit length. Then, given a image patch P with the size of $2\omega \times 2\omega$, whose center is located at (x_p, y_p) , its local distribution can be expressed as:

$$S_{P,\omega}(x, y) = \mathcal{L}(x - x_p, y - y_p; H_P) \quad (2)$$

where $x \in [x - \omega, x + \omega]$, $y \in [y - \omega, y + \omega]$, \mathcal{L} denotes a parameterized mathematical model to describe the local distribution, and H_P denotes the corresponding parameters to formulate \mathcal{L} .

Assuming the sampling points in the HR image are $\{(x_{p1}, y_{p1}), (x_{p2}, y_{p2}), \dots, (x_{pk}, y_{pk})\}$, we can easily calculate all observed pixels with Equation (2). Given a specific upsampling factor s and the corresponding matrix M_s , the observed k HR pixels of the corresponding region of the LR patch P can be quickly located in M_s . Enlarging the patch size and conducting the overlapped calculation are widely adopted by traditional methods [31]. However, such strategy is quite inefficient in CNN-based methods. Inspired by [19], we adopt a pixel-wise local reconstruction strategy. As shown in Figure 1, each local patch contains one pixel in the LR image and the corresponding sub-pixel in the HR image. In this way, the reconstruction area and sampling points are both minimized, which could significantly simplify the local distribution reconstruction and avoid redundant sampling calculations.

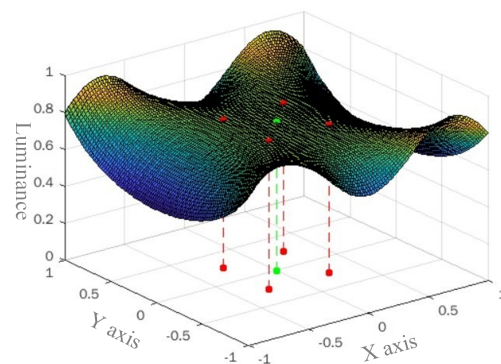


Figure 1. The local distribution of an LR pixel in situation. The green point denotes the pixel in the LR image, and the red point denotes the corresponding sub-pixels in the HR image.

2.2. Local Distribution Reconstruction

Linear models, polynomial models, frequency models and Gaussian models are widely used mathematical models for describing the local image distribution and estimating the sub-pixels [32–36]. However, estimating the real scene's distribution is a ill-posed problem. The above simple mathematical models struggle to precisely describe the real scene. Inspired by artificial neural networks, we introduce a multi-layer neural network operator (MNNO) to approach the real scene's distribution.

As shown in Figure 2, the MNNO is a multi-layer full connection neural network. As argued in Equation (2), the MNNO takes the 2D coordinate of the sampling point as the input and then outputs a c -channel sampling value, where $c = 1$ is for gray pixels and $c = 3$ is for color pixels. In this situation, the local distribution is certainly determined by

the parameters of MNNO. Assuming MNNO is formulated by N full connection layers, for the i -th layer, its input and output are denoted as f_i and f_{i+1} , respectively. Then, the process of the i -th layer can be expressed as:

$$f_{i+1} = \mathcal{FC}(f_i, H_i) = \begin{cases} \sigma(f_i \circ H_i) & i < N \\ f_i \circ H_i & i = N \end{cases} \quad (3)$$

where \mathcal{FC} denotes the process of a full connection layer, σ denotes the activation function, \circ refers to matrix multiplication and H_i denotes the parameter matrix of the i -th layer. Specifically, the calculation of the i -th full connection layer can be expressed as:

$$f_{i+1}^u = \sum_v f_i^v \cdot h_i^{u,v} \quad (4)$$

where u and v are the channel indexes of f_{i+1} and f_i , respectively, and $h_i^{u,v}$ is the element at (u, v) of H_i .

Assuming f_i and f_{i+1} obtains n_i and n_{i+1} channels, respectively, the size of H_i can be obtained by $n_i \cdot n_{i+1}$. Then, the complete process of MNNO can be expressed as:

$$\text{MNNO}([x_{pj}, y_{pj}]) = \mathcal{FC}(\dots \mathcal{FC}([x_{pj} - x_P, y_{pj} - y_P], H_1) \dots, H_N) + H_{bias} \quad (5)$$

where H_{bias} receives the same channel number of the output pixel. We denote the MNNO formulated by such N full connection layers as $\text{MNNO}^{\{n_1, n_2, \dots, n_N\}}$. Therefore, the total parameters of the MNNO can be obtained as:

$$T(\text{MNNO}^{\{n_1, n_2, \dots, n_N\}}) = c + \sum_{i=1}^N n_i \cdot n_{i+1} \quad (6)$$

where $n_1 = 2, n_{N+1} = c$ and T is a function returning the total of the parameters in the model.

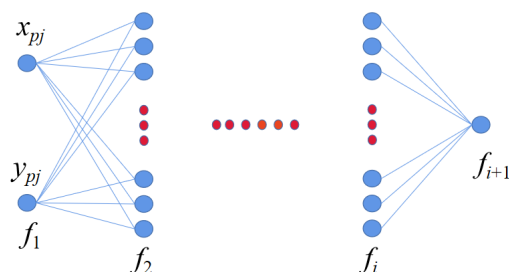


Figure 2. The proposed multi-layer neural network operator (MNNO) takes two-dimensional sampling coordinate points as input and outputs sampling values.

Unlike traditional CNN-based SISR methods that directly output the reconstructed HR pixels, we adopt a CNN backbone to estimate the parameters of the MNNO for each pixel.

2.3. Sampling Matrix

As argued in the previous subsection, the neighborhood of each pixel is only supposed to cover the corresponding sub-pixels in the HR image. It is clear that given a random float upsampling factor, the sub-pixels' relative position in a local patch are probably different from other patches. However, for integer upsampling factors, the situations will be much simpler. Given a integer upsampling factor s , one LR pixel can be uniformly divided into s^2 sub-pixels. Assuming the origin is at the LR pixel, the relative coordinates of the sub-pixel at the i -th column and j -th row can be easily calculated by the symmetry principle as:

$$(\hat{x}_i, \hat{y}_j) = \left(\frac{2i - s - 1}{2s}, \frac{2j - s - 1}{2s} \right) \quad (7)$$

where (\hat{x}_i, \hat{y}_j) denotes the relative coordinates. Then, we can obtain an $s^2 \times 2$ -sized coordinate matrix for each LR pixel.

2.4. Overview of the Architecture

Figure 3 illustrates the architecture of the proposed LDRN. The proposed method consists of two parts: the CNN backbone and the distribution reconstruction module (DRM). The CNN backbone is supposed to estimate the parameters for constructing the local distributions. The DRM then reconstructs the sub-pixels using Equations (3) and (5) and finally outputs the HR image via the pixel shuffle operation.

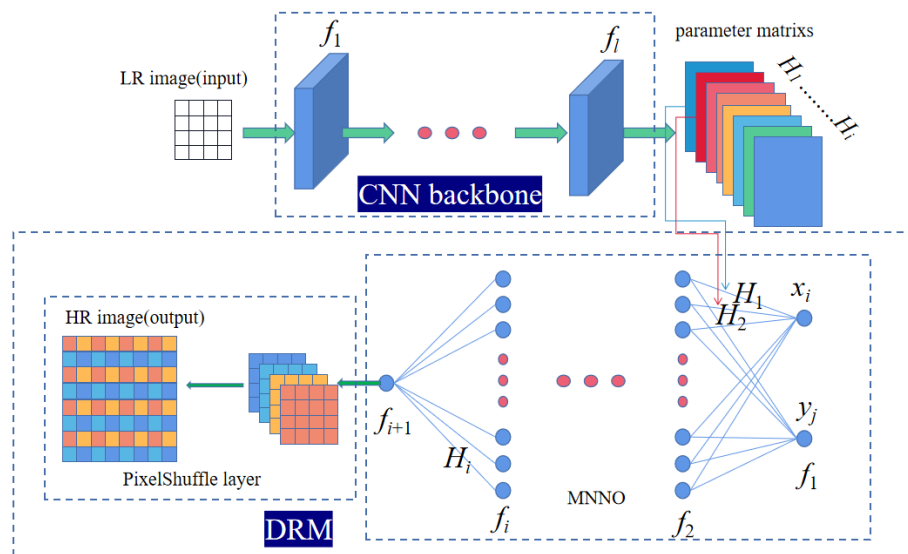


Figure 3. The proposed LDRN consists of the CNN backbone and the DRM. The CNN backbone is used to generate the parameter matrix, and the DRM is used to generate the HR image.

The recurrent-like architectures [37–39] are widely adopted by SISR methods to formulate the backbone. Though they exhibit outstanding performance, they clearly suffer from the expensive computation cost resulting from the multiple residual convolution blocks. For instance, typical light recurrent networks such as EDSR-baseline [40], SRResnet [41], etc., obtain over millions of parameters and take over 2.8 trillion Flops to process a 1920×1080 -sized image. Even the much more efficient VDSR [42] is also too large to be implemented on the hardware platforms [30]. To achieve extreme efficiency, we only adopt a few convolution layers to construct the baseline. Assuming the CNN backbone is formulated by L convolution layers, these L convolution layers are sequentially stacked. For the l -th layer, f^l and f^{l+1} are recorded as its input and output. Then, the process of the l -th layer can be expressed as:

$$f^{l+1} = \mathcal{CN}(f^l, W_l, B_l) = \begin{cases} \sigma(0, W_l * f^l + B_l) & l < L \\ W_l * f^l + B_l & l = L \end{cases} \tag{8}$$

where W_l and B_l denote the convolution kernel and bias of the i -th layer, and $*$ denotes the convolution operation. As a 2D convolution kernel, the shape of W_l can be written as $c_{l-1} \times c_l \times k_l \times k_l$, where c_l denotes the channel size of the output of the l -th layer and k_l denotes the size of square kernel.

The DRM is supposed to conduct MNNO to obtain the final sub-pixels for each LR pixel via the sampling matrix and the parameters estimated by the CNN backbone. Then, these sub-pixels are re-arranged by the shuffling operation to reconstruct the final HR image. As described in Equation (5), using a larger N and larger n_i to formulate the MNNO could help to approach a more complex and non-linear distribution. However, this will also introduce too high of a computation cost and make the algorithm quite inefficient.

Moreover, the vanishing gradient is another serious challenge for a deep full connection neural network. To solve these two problems, we adopt a shallow and small-scale MNNO to formulate the DRM. First, the small-scale MNNO could save lots of parameters and computation. Second, the shallow depth could ensure back-propagating the gradient to the shallow layers of the CNN backbone and avoid the vanishing gradient.

2.5. Implementation Details

The proposed LDRN consists of a CNN backbone and DRM. For the CNN backbone, we set $L = 4$, $(k_1, c_1) = (5, 64)$, $(k_2, c_2) = (3, 32)$, $(k_3, c_3) = (3, 32)$, $(k_4, c_4) = (3, T(MNNO\{n_1, n_2, \dots, n_N\}))$. To keep the size of the input LR image unchanged, we set the padding size of the l -th layer to $\frac{k_l-1}{2}$. As described in Section 2.4, we adopt shallow and small-scale settings for the DRM, so we set $N = 2$ and $\{n_1, n_2\} = \{12, 1\}$. Therefore, we can easily obtain that $c_4 = 37$ based on Equation (6). Moreover, we adopt *PReLU* as the activation function for the CNN backbone and *ReLU* as the activation function for the DRM. With the above settings, the proposed method has 40k parameters in total.

To train the proposed LDRN, we adopt the DIV2K [43] as the training dataset and Set5 [44] as the validation set. The LR images are generated using Bicubic interpolation. The 32×32 pixel I^{LR} patches are extracted from I^{LR} sub-images, and $32s \times 32s$ pixel I^{HR} patches are extracted from I^{HR} sub-images. The details of obtaining I^{LR} and I^{HR} will be extended in Section 3.1. We utilized random clipping to augment the training patches. Like previous studies, we transformed each patch into YCbCr space and only trained on the Y-channel. To train our model, we adopt Adam [45] as the optimizer and set the batchsize to 32. The learning rate is initialized to 10^{-3} . We test the PSNR performance on the validation set after the end of each training epoch. The learning rate will be halved when the PSNR performance on validation does not increase for 10 consecutive epochs. The minimum learning rate is set to 10^{-6} , and the maximum training epochs is set to 200. When the minimum learning rate is achieved or when the maximum training epoch is finished, the training will immediately stop. We choose the L1 loss as the loss function. The training takes roughly 90 min on a 2080Ti GPU. The PSNR is also used as the performance metric to evaluate our model. For each upscaling factor, we train a specific network. It is worth mentioning that because of the good Adam optimizer and the mature training strategy, the performance fluctuation of each method is less than 0.01 dB and hardly affects the comparison results. Therefore, we will not report the confidence intervals of the results in the following experiments.

3. Experiments

In this section, we evaluate the performance of the proposed method using five benchmark datasets. First, we describe the five benchmark datasets in detail. Then, we demonstrate the effectiveness of the proposed CNN backbone and DRM. Moreover, we also show that the settings given in Section 2.5 are the most appropriate settings for the proposed method. Finally, we compare the proposed method with several extremely efficient SISR methods to demonstrate the superiority of the proposed method.

3.1. Datasets

To train the proposed method, we adopt a training set from the DIV2K dataset as the training dataset, which contains 800 HR images with 2K resolution. To obtain the LR images, we downsample the HR images using bicubic kernels with a scale factor of $s \in \{2, 3, 4\}$. We group the I^{HR} into 192×192 -sized patches with a stride of 192 and crop I^{LR} patches to the size of $\frac{192}{s} \times \frac{192}{s}$ from the corresponding LR image with a stride of $\frac{192}{s}$. In this way, we obtain 55510 non-overlapped training data pairs in total. In the testing stage, we introduced five widely used public datasets, including the Set5, Set14 [46], B100 [47], Urban100 [48] and Manga109 [49], to evaluate the performance of the proposed method and compared methods.

3.2. Ablation Investigation

In this subsection, we demonstrate the contribution of the proposed components, including the CNN backbone and the distribution reconstruction module, in detail.

3.2.1. CNN Backbone

We first compare the performance of the proposed CNN backbone with several existing backbones adopted by extremely efficient SISR methods, including SRCNN [11], ESPCN [19] and FSRCNN [50].

As shown in Table 1, the proposed backbone clearly surpasses existing backbones for all datasets. Especially on the most challenging datasets Manga109 and Urban100, the proposed backbone beats the second-best FSRCNN backbone by over 0.1 dB. The SRCNN's backbone introducing large-sized convolution kernel does not provide positive effects for local distribution learning. Though FSRCNN's backbone obtains the least parameters, it suffers from the poor receptive field of the 1×1 -sized convolution kernel, which cannot provide much information to support reconstructing the local distribution.

Table 1. The comparison of PSNR and SSIM [51] with different CNN backbone settings on benchmark datasets. Bold indicates the best performance, while Underline indicates the second best.

Dataset	Scale	SRCNN Backbone	FSRCNN Backbone	ESPCN Backbone	Ours Backbone
Set5	$\times 2$	37.10/0.9807	<u>37.21/0.9809</u>	36.62/0.9792	37.35/0.9812
	$\times 3$	33.57/0.9647	<u>33.80/0.9622</u>	33.13/0.9612	33.81/0.9663
	$\times 4$	30.59/0.9315	<u>30.77/0.9343</u>	30.19/0.9252	30.81/0.9349
Set14	$\times 2$	32.63/0.9506	<u>32.73/0.9509</u>	32.33/0.9487	32.84/0.9514
	$\times 3$	29.70/0.9104	<u>29.86/0.9119</u>	29.47/0.9069	29.88/0.9122
	$\times 4$	27.44/0.8594	<u>27.58/0.8619</u>	27.21/0.8539	27.62/0.8626
B100	$\times 2$	33.53/0.9534	<u>33.41/0.9536</u>	33.03/0.9512	33.49/0.9514
	$\times 3$	28.99/0.8843	<u>29.09/0.8856</u>	28.76/0.8805	29.13/0.8863
	$\times 4$	27.81/0.8478	<u>27.89/0.8493</u>	27.61/0.8429	27.93/0.8501
Urban100	$\times 2$	30.00/0.9385	<u>30.17/0.9397</u>	29.34/0.9315	30.36/0.9417
	$\times 3$	27.29/0.8914	<u>27.51/0.8954</u>	26.84/0.8827	27.61/0.8971
	$\times 4$	24.51/0.8167	<u>24.68/0.8220</u>	24.22/0.8065	24.73/0.8239
Manga109	$\times 2$	36.92/0.9864	<u>37.20/0.9869</u>	35.89/0.9839	37.45/0.9873
	$\times 3$	31.03/0.9559	<u>31.48/0.9591</u>	30.16/0.9481	31.60/0.9601
	$\times 4$	28.09/0.9199	<u>28.45/0.9254</u>	27.41/0.9090	28.57/0.9270

3.2.2. Distribution Reconstruction Module

The distribution reconstruction module (DRM) is the core module in achieving the super resolution. As argued in Section 2.4, a deeper neural network in MNNO would suffer from gradient back-propagation and cannot achieve a better performance. We show the training loss curves and validation PSNR curves using $N = \{12, 1\}$, $N = \{5, 5, 1\}$ and $N = \{10, 10, 1\}$ settings in Figure 4. The $N = \{5, 5, 1\}$ setting obtains a closed number of parameters to $N = \{12, 1\}$. Comparing the curves of $N = \{12, 1\}$ and $N = \{5, 5, 1\}$, using a similar scale of parameters to construct a deeper neural network cannot achieve a better performance. Moreover, from the results of $N = \{10, 10, 1\}$, using much more parameters to construct a deeper neural network also provides little help in improving the performance. Therefore, we adopt a two-layer neural network in MNNO to formulate the DRM.

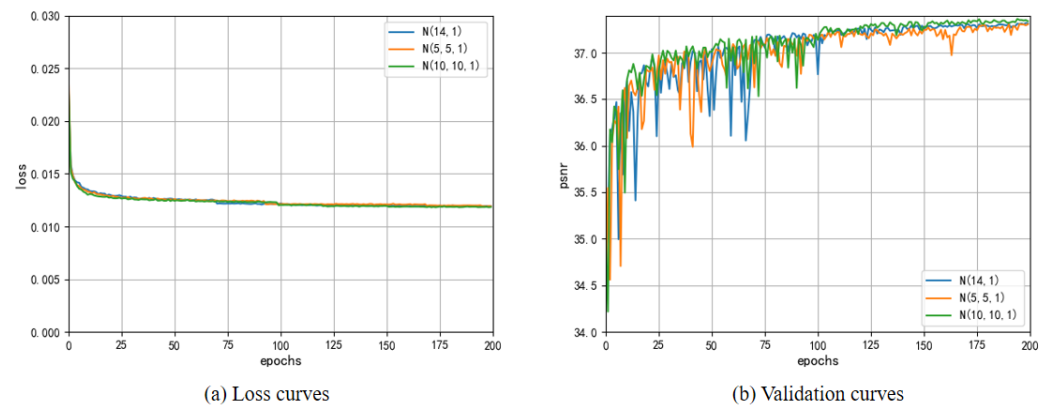


Figure 4. Training curves for $N = (12,1)$, $N = (5,5,1)$ and $N = (10,10,1)$.

Then, we investigate the best settings for a two-layer neural network. We construct a group of models with different MNNO settings that include $N = 0$, $N = \{4, 1\}$, $N = \{6, 1\}$, \dots , $N = \{20, 1\}$, where $N = 0$ denotes the model using only a convolution layer rather than MNNO to output sub-pixels. From the results shown in Table 2, using small-scale settings to construct MNNO shows closed performances to a normal convolution layer. However, the larger MNNO does not always lead to a better performance. The larger MNNO leads to a more complex distribution model, which certainly increases the difficulty of estimating the MNNO parameters. Observing that the setting $N = \{12, 1\}$ achieves the best balance between complexity and performance, we adopt $N = \{12, 1\}$ setting to formulate the DRM.

Table 2. The comparison of PSNR and SSIM of different N settings with upsampling factor 2 on benchmark datasets. Bold indicates the best performance, while Underline indicates the second best.

Dataset	$N = 0$	$N = (4,1)$	$N = (6,1)$	$N = (8,1)$	$N = (10,1)$	$N = (12,1)$	$N = (14,1)$	$N = (16,1)$	$N = (18,1)$	$N = (20,1)$
Set5	37.26	37.26	37.28	37.31	37.34	<u>37.35</u>	<u>37.35</u>	37.36	37.34	<u>37.35</u>
Set14	32.80	32.81	32.81	<u>32.86</u>	<u>32.86</u>	32.88	32.84	32.84	32.88	32.83
B100	33.47	33.46	33.47	33.49	<u>33.50</u>	33.51	33.49	<u>33.50</u>	33.51	33.49
Urban100	30.23	30.25	30.31	30.33	30.40	<u>30.41</u>	30.36	<u>30.41</u>	30.43	30.36
Manga109	37.25	37.36	37.32	37.40	<u>37.49</u>	37.50	37.45	37.44	37.48	37.36

3.3. Comparison with State-of-the-Art Methods

To fairly evaluate the performance of the proposed method, we compare the method with three typical, extremely efficient SISR methods, including SRCNN, FSRCNN and ESPCN, and another two recently proposed methods—HFSR [30] and TSSRN [29]. We retrained all compared methods using the same training strategy to ensure fair comparisons. Because HFSR [30] could only be applied on a $\times 2$ scale, we only train the HFSR for a $\times 2$ scale comparison.

For an objective evaluation, we calculate the PSNR and SSIM for different upscaling factors on five benchmark datasets. The quantitative results are shown in Table 3. The proposed method outperforms both $\times 2$ (0.244 dB higher than the second average) and $\times 3$ (0.106 dB higher than the second best) on five benchmark datasets of all compared methods. Although the proposed method is not the best in terms of $\times 4$ (lower than the first average by 0.032 dB), the gap is very small and does not exceed 0.04 dB on average. To further illustrate the effects of different downsampling methods, we conduct an additional experiment by producing the LR images with Gaussian downsampling. Specifically, the Gaussian downsampling firstly blurs the HR image with a 3×3 Gaussian blur kernel and then downsamples the blurred image with a mean filter. Table 4 shows the comparison

result. Comparing the bicubic results shown in Tables 3 and 4, the Gaussian downsampling produces more serious LR degradation. Obviously, TSSRN obtains relatively good results for bicubic downsampling degradation and exhibits poor performance on the Gaussian downsampling degradation. By contrast, our LDRN achieves even greater performance gain from the bicubic interpolation. This observation certainly demonstrates that the proposed distribution learning architecture is robust to tougher situations.

Moreover, we also provide the results of the subjective evaluation for the more challenging $\times 3$ and $\times 4$ scales, respectively, in Figures 5 and 6. Because the HFSR can only process $\times 2$ scaled images, it will not be included in this comparison. In the more challenging Urban100 and Manga109 datasets, our LDRN exhibits better detailed reconstruction ability caused by the MNNO.

To fully investigate the efficiency of all compared methods, we list the running times, parameters, FLOPs and memory costs of all compared methods for processing a 1920×1080 -sized image on the RTX 2080Ti GPU in Table 5. We also include typical efficient SISR methods VDSR [42] and EDSR [40] as references in the comparison. Compared to other methods, these two efficient methods have unaffordable computation and memory costs—VDSR requires 9.3 GB memory, and EDSR takes over 2.8T FLOPs and 244 ms to process a 1920×1080 sized images. As far as we know, other efficient SISR methods [24,25,52] (also called as lightweight methods) always achieve similar efficiencies between EDSR and VDSR. In contrast, the other methods contain less than 50k parameters and consume less than 3 GB memory for the same processing except for SRCNN. Accordingly, we can conclude the extreme efficiencies of these methods. Our method has a close running speed to HFSR and close memory cost to ESPCN, which certainly satisfies real-time processing. However, our LDRN contains the most parameters and the second most flops among these extremely efficient methods due to the MNNO.

Table 3. The results of PSNR and SSIM on public benchmark datasets (Bicubic). Bold indicates the best performance, while Underline indicates the second best.

Dataset	Scale	Bicubic	SRCNN ECCV'14	FSRCNN ECCV'16	ESPCN CVPR'16	HFSR TCSVT'19	TSSRN JETCAS'20	LDRN Proposed
Set5	$\times 2$	33.68/0.9644	36.83/0.9798	37.09/0.9806	36.82/0.9797	37.13/0.9807	<u>37.18/0.9808</u>	37.35/0.9812
	$\times 3$	30.90/0.9366	33.37/0.9633	33.78/0.9660	33.42/0.9632	-/-	<u>33.78/0.9662</u>	33.86/0.9666
	$\times 4$	28.46/0.8918	30.45/0.9298	<u>30.84/0.9350</u>	30.48/0.9291	-/-	30.87/0.9355	30.82/0.9349
Set14	$\times 2$	30.23/0.9260	32.46/0.9495	32.68/0.9505	32.46/0.9494	32.67/0.9505	<u>32.71/0.9507</u>	32.88/0.9516
	$\times 3$	27.89/0.8785	29.60/0.9090	<u>29.87/0.9117</u>	29.65/0.9090	-/-	29.84/0.9115	29.92/0.9125
	$\times 4$	25.99/0.8219	27.34/0.8573	<u>27.61/0.8617</u>	27.40/0.8578	-/-	27.64/0.8624	<u>27.61/0.8624</u>
B100	$\times 2$	30.95/0.9266	33.20/0.9522	33.34/0.9532	33.16/0.9519	33.36/0.9532	<u>33.39/0.9535</u>	33.51/0.9543
	$\times 3$	27.65/0.8520	28.91/0.8829	<u>29.09/0.8854</u>	28.89/0.8823	-/-	29.08/0.8854	29.14/0.8865
	$\times 4$	26.70/0.8142	27.74/0.8453	<u>27.92/0.8493</u>	27.74/0.8459	-/-	27.94/0.8497	<u>27.92/0.8498</u>
Urban100	$\times 2$	26.89/0.8935	29.68/0.9355	29.95/0.9380	29.49/0.9332	29.97/0.9384	<u>30.05/0.9391</u>	30.41/0.9422
	$\times 3$	25.22/0.8406	27.20/0.8891	27.51/0.8944	27.08/0.8864	-/-	<u>27.51/0.8947</u>	27.64/0.8978
	$\times 4$	23.17/0.7631	24.47/0.8140	24.69/0.8214	24.42/0.8124	-/-	<u>24.73/0.8223</u>	24.73/0.8238
Manga109	$\times 2$	31.27/0.9628	36.39/0.9851	37.02/0.9864	36.46/0.9850	37.05/0.9865	<u>37.10/0.9866</u>	37.50/0.9875
	$\times 3$	27.27/0.9123	30.78/0.9536	31.46/0.9585	30.71/0.9521	-/-	<u>31.49/0.9587</u>	31.67/0.9604
	$\times 4$	25.30/0.8655	27.95/0.8173	28.50/0.9252	27.89/0.9158	-/-	28.63/0.9266	<u>28.57/0.9270</u>

Table 4. The results of PSNR and SSIM on public benchmark datasets (Gaussian). Bold indicates the best performance, while Underline indicates the second best.

Dataset	Scale	Bicubic	SRCNN	FSRCNN	ESPCN	HFSR	TSSRN	LDRN
Set5	×2	32.10/0.9517	36.71/0.9793	<u>36.99/0.9803</u>	36.64/0.9791	36.55/0.9788	35.57/0.9754	37.24/0.9809
	×3	30.27/0.9292	33.35/0.9633	<u>33.64/0.9654</u>	33.27/0.9624	-/-	32.03/0.9518	33.69/0.9658
	×4	28.18/0.8884	30.39/0.9298	<u>30.61/0.9330</u>	30.27/0.9269	-/-	29.82/0.9207	30.72/0.9345
Set14	×2	29.02/0.9054	32.39/0.9489	<u>32.59/0.9502</u>	32.29/0.9486	32.12/0.9465	31.53/0.9428	32.85/0.9515
	×3	27.48/0.8696	29.50/0.9083	<u>29.70/0.9101</u>	29.52/0.9077	-/-	28.72/0.8982	29.73/0.9109
	×4	25.50/0.8091	27.22/0.8561	<u>27.37/0.8580</u>	27.18/0.8543	-/-	26.32/0.8369	27.45/0.8605
B100	×2	29.73/0.9038	33.15/0.9519	<u>33.33/0.9532</u>	33.05/0.9511	32.80/0.9483	32.30/0.9451	33.48/0.9542
	×3	27.35/0.8429	28.85/0.8820	<u>28.94/0.8832</u>	28.74/0.8803	-/-	28.22/0.8725	28.99/0.8847
	×4	26.56/0.8115	27.67/0.8453	<u>27.73/0.8465</u>	27.61/0.8442	-/-	27.36/0.8395	27.82/0.8485
Urban100	×2	25.87/0.8679	29.57/0.9341	<u>29.95/0.9377</u>	29.40/0.9319	29.35/0.9323	28.14/0.9187	30.37/0.9418
	×3	24.88/0.8303	27.15/0.8889	<u>27.40/0.8929</u>	26.98/0.8855	-/-	25.93/0.8664	27.59/0.8978
	×4	23.04/0.7604	24.43/0.8154	<u>24.59/0.8203</u>	24.28/0.8103	-/-	23.92/0.8010	24.71/0.8254
Manga109	×2	29.38/0.9461	36.32/0.9846	<u>37.09/0.9864</u>	36.29/0.9845	36.31/0.9845	34.41/0.9790	37.43/0.9872
	×3	26.74/0.9045	30.74/0.9537	<u>31.38/0.9582</u>	30.58/0.9517	-/-	28.55/0.9335	31.56/0.9600
	×4	23.14/0.8248	27.71/0.9156	<u>28.21/0.9225</u>	27.50/0.9120	-/-	23.19/0.8430	28.32/0.9247

Table 5. The results of running time evaluation and parameters.

Method	SRCNN	ESPCN	FSRCNN	HFSR	TSSRN	VDSR	EDSR	LDRN
Parameters	57k	21k	13k	20k	14k	680k	1368k	40k
Time (ms)	0.91	0.49	0.81	1.02	0.60	1.64	244.21	1.16
FLOPs	475.1G	44.1G	54.4G	41.5G	44.7G	6124.9G	2839.3G	83.1G
Memory (GB)	5.2	2.6	2.9	2.1	2.3	9.3	7.2	2.6

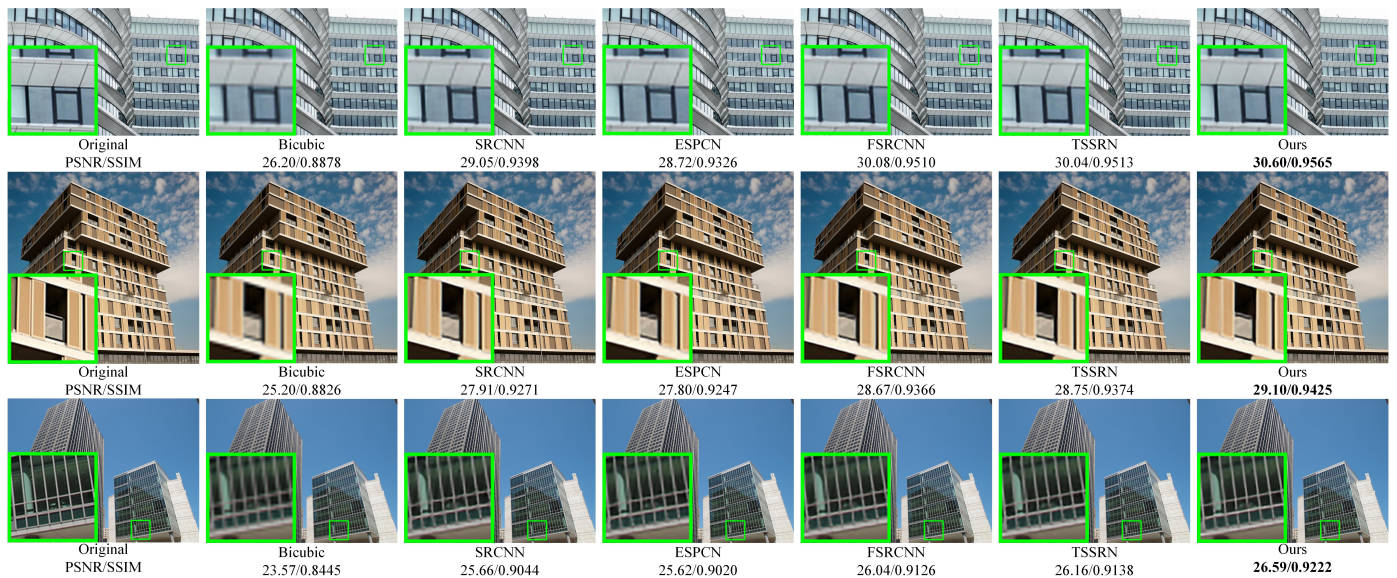


Figure 5. The “052”, “087” and “096” images from the Urban100 dataset with an upscaling factor of 3.



Figure 6. The “HsuguruHaru_vol20”, “AosuguruHaru” and “Nekodama” images from the Manga109 dataset with an upscaling factor of 4.

4. Conclusions

In this paper, we propose a novel local distribution reconstruction network for extremely efficient single-image super-resolution. The proposed method consists of a CNN backbone and a distribution reconstruction module. To achieve extreme efficiency, we adopt a four-layer CNN to formulate the backbone. In the distribution reconstruction module, we propose a multi-layer neural network operator to approach the distribution model of the real scene and calculate the HR pixels by sampling. The ablation study demonstrates the effectiveness of the proposed CNN backbone and MNNO. The experiments on two downsampling methods show that the proposed method exhibits the ability to solve different kinds of LR degradation and clearly beats the second-best method with large margins (over 0.244 dB for $\times 2$ in average) for more challenging Gaussian downsampling. Overall, the proposed method presents good performance and efficiency and shows a promising performance when deployed on hardware platforms.

Author Contributions: Conceptualization, W.W. and B.Z.; methodology, W.W. and B.Z.; software, W.X.; validation, W.W. and B.Z.; formal analysis, W.W. and A.H.; investigation, W.W., W.X. and A.H.; resources, W.W. and W.X.; data curation, W.X.; writing—original draft preparation, W.W., W.X. and B.Z.; writing—review and editing, B.Z.; visualization, W.X.; supervision, C.Y.; project administration, W.W. and B.Z.; funding acquisition, W.W. and B.Z. All authors have read and agreed to the published version of the manuscript.

Funding: This research is funded by National Nature Science Foundation of China (61501154, 62001146), and the APC is funded by National Nature Science Foundation of China (61501154).

Institutional Review Board Statement: Our study does not require ethical approval.

Informed Consent Statement: Our study does not involve humans.

Data Availability Statement: The research project will be available at <https://github.com/XuWen666/LDRN> (accessed on 11 March 2022).

Conflicts of Interest: The authors declare that there is no conflict of interest exists in this research.

References

1. Zhou, F.; Yang, W.; Liao, Q. Interpolation-based image super-resolution using multisurface fitting. *IEEE Trans. Image Process.* **2012**, *21*, 3312–3318. [[CrossRef](#)]
2. Gilman, A.; Bailey, D.G.; Marsland, S.R. Interpolation models for image super-resolution. In Proceedings of the 4th IEEE International Symposium on Electronic Design, Test and Applications (Delta 2008), Hong Kong, China, 23–25 January 2008; pp. 55–60.
3. Mallat, S.; Yu, G. Super-resolution with sparse mixing estimators. *IEEE Trans. Image Process.* **2010**, *19*, 2889–2900. [[CrossRef](#)]
4. Chappalli, M.B.; Bose, N.K. Simultaneous noise filtering and super-resolution with second-generation wavelets. *IEEE Signal Process. Lett.* **2005**, *12*, 772–775. [[CrossRef](#)]
5. Lo, K.H.; Wang, Y.C.F.; Hua, K.L. Joint trilateral filtering for depth map super-resolution. In Proceedings of the 2013 Visual Communications and Image Processing (VCIP), Kuching, Malaysia, 17–20 November 2013; pp. 1–6.
6. Mei, Y.; Fan, Y.; Zhou, Y. Image super-resolution with non-local sparse attention. In Proceedings of the IEEE/CVF Conference on Computer Vision and Pattern Recognition, Nashville, TN, USA, 20–25 June 2021; pp. 3517–3526.
7. Bendory, T.; Dekel, S.; Feuer, A. Super-resolution on the sphere using convex optimization. *IEEE Trans. Signal Process.* **2015**, *63*, 2253–2262. [[CrossRef](#)]
8. Ng, M.K.; Bose, N.K. Mathematical analysis of super-resolution methodology. *IEEE Signal Process. Mag.* **2003**, *20*, 62–74. [[CrossRef](#)]
9. Sun, L.; Hays, J. Super-resolution from internet-scale scene matching. In Proceedings of the 2012 IEEE International Conference on Computational Photography (ICCP), Seattle, WA, USA, 28–29 April 2012; pp. 1–12.
10. Qu, Y.Y.; Liao, M.J.; Zhou, Y.W.; Fang, T.Z.; Lin, L.; Zhang, H.Y. Image super-resolution based on data-driven Gaussian process regression. In *International Conference on Intelligent Science and Big Data Engineering*; Springer: Berlin, Germany, 2013; pp. 513–520.
11. Dong, C.; Loy, C.C.; He, K.; Tang, X. Learning a deep convolutional network for image super-resolution. In Proceedings of the ECCV, Zurich, Switzerland, 6–12 September 2014.
12. Yang, S.; Wang, M.; Chen, Y.; Sun, Y. Single-image super-resolution reconstruction via learned geometric dictionaries and clustered sparse coding. *IEEE Trans. Image Process.* **2012**, *21*, 4016–4028. [[CrossRef](#)]
13. Gu, S.; Zuo, W.; Xie, Q.; Meng, D.; Feng, X.; Zhang, L. Convolutional sparse coding for image super-resolution. In Proceedings of the IEEE International Conference on Computer Vision, Santiago, Chile, 7–13 December 2015; pp. 1823–1831.
14. Wang, Z.; Liu, D.; Yang, J.; Han, W.; Huang, T. Deep Networks for Image Super-Resolution with Sparse Prior. In Proceedings of the ICCV, Santiago, Chile, 7–13 December 2015; pp. 370–378. [[CrossRef](#)]
15. Yamashita, R.; Nishio, M.; Do, R.K.G.; Togashi, K. Convolutional neural networks: An overview and application in radiology. *Insights Into Imaging* **2018**, *9*, 611–629. [[CrossRef](#)]
16. Yang, X.; Mei, H.; Zhang, J.; Xu, K.; Yin, B.; Zhang, Q.; Wei, X. DRFN: Deep recurrent fusion network for single-image super-resolution with large factors. *IEEE Trans. Multimed.* **2018**, *21*, 328–337. [[CrossRef](#)]
17. Hui, Z.; Wang, X.; Gao, X. Two-stage convolutional network for image super-resolution. In Proceedings of the 2018 24th International Conference on Pattern Recognition (ICPR), IEEE, Beijing, China, 20–24 August 2018; pp. 2670–2675.
18. Ronneberger, O.; Fischer, P.; Brox, T. U-Net: Convolutional Networks for Biomedical Image Segmentation. In Proceedings of the International Conference on Medical Image Computing and Computer-assisted Intervention, Munich, Germany, 5–9 October 2015.
19. Shi, W.; Caballero, J.; Huszar, F.; Totz, J.; Aitken, A.P.; Bishop, R.; Rueckert, D.; Wang, Z. Real-Time Single Image and Video Super-Resolution Using an Efficient Sub-Pixel Convolutional Neural Network. In Proceedings of the CVPR, IEEE, Las Vegas, NV, USA, 27–30 June 2016. [[CrossRef](#)]
20. Arirangan, S.; Kottursamy, K. Multi-scaled feature fusion enabled convolutional neural network for predicting fibrous dysplasia bone disorder. *Expert Syst.* **2021**, e12882. [[CrossRef](#)]
21. Saranya, A.; Kottursamy, K.; AlZubi, A.A.; Bashir, A.K. Analyzing fibrous tissue pattern in fibrous dysplasia bone images using deep R-CNN networks for segmentation. *Soft Comput.* **2021**, 1–15. [[CrossRef](#)]
22. Lan, R.; Sun, L.; Liu, Z.; Lu, H.; Pang, C.; Luo, X. MADNet: A fast and lightweight network for single-image super resolution. *IEEE Trans. Cybern.* **2020**, *51*, 1443–1453. [[CrossRef](#)]
23. Chudasama, V.; Prajapati, K.; Upla, K. Computationally efficient super-resolution approach for real-world images. In Proceedings of the National Conference on Computer Vision, Pattern Recognition, Image Processing, and Graphics, Hubballi, India, 22–24 December 2019; Springer: Berlin, Germany, 2019; pp. 143–153.

24. Liu, J.; Zhang, W.; Tang, Y.; Tang, J.; Wu, G. Residual feature aggregation network for image super-resolution. In Proceedings of the IEEE/CVF Conference on Computer Vision and Pattern Recognition, Seattle, WA, USA, 13–19 June 2020; pp. 2359–2368.
25. Zhang, Y.; Wei, D.; Qin, C.; Wang, H.; Pfister, H.; Fu, Y. Context reasoning attention network for image super-resolution. In Proceedings of the IEEE/CVF International Conference on Computer Vision, Montreal, QC, Canada, 10–17 October 2021; pp. 4278–4287.
26. Zhang, K.; Gool, L.V.; Timofte, R. Deep unfolding network for image super-resolution. In Proceedings of the IEEE/CVF Conference on Computer Vision and Pattern Recognition, Seattle, WA, USA, 13–19 June 2020; pp. 3217–3226.
27. Prajapati, K.; Chudasama, V.; Patel, H.; Upla, K.; Raja, K.; Ramachandra, R.; Busch, C. Direct Unsupervised Super-Resolution Using Generative Adversarial Network (DUS-GAN) for Real-World Data. *IEEE Trans. Image Process.* **2021**, *30*, 8251–8264. [[CrossRef](#)]
28. Prajapati, K.; Chudasama, V.; Patel, H.; Upla, K.; Raja, K.; Ramachandra, R.; Busch, C. Unsupervised Real-World Super-resolution Using Variational Auto-encoder and Generative Adversarial Network. In Proceedings of the International Conference on Pattern Recognition, Virtual, 4–6 February 2021; Springer: Berlin, Germany, 2021; pp. 703–718.
29. Lee, J.; Lee, J.; Yoo, H.J. SRNPU: An Energy-Efficient CNN-Based Super-Resolution Processor With Tile-Based Selective Super-Resolution in Mobile Devices. *IEEE J. Emerg. Sel. Top. Circuits Syst.* **2020**, *10*, 320–334. [[CrossRef](#)]
30. Kim, Y.; Choi, J.S.; Kim, M. A Real-Time Convolutional Neural Network for Super-Resolution on FPGA With Applications to 4K UHD 60 fps Video Services. *IEEE Trans. Circuits Syst. Video Technol.* **2019**, *29*, 2521–2534. [[CrossRef](#)]
31. Dabov, K.; Foi, A.; Katkovnik, V.; Egiazarian, K. Image Denoising by Sparse 3-D Transform-Domain Collaborative Filtering. *IEEE Trans. Image Process.* **2007**, *16*, 2080–2095. [[CrossRef](#)]
32. Zheng, B.; Chen, Y.; Tian, X.; Zhou, F.; Liu, X. Implicit dual-domain convolutional network for robust color image compression artifact reduction. *IEEE Trans. Circuits Syst. Video Technol.* **2019**, *30*, 3982–3994. [[CrossRef](#)]
33. Zheng, B.; Yuan, S.; Slabaugh, G.; Leonardis, A. Image demoireing with learnable bandpass filters. In Proceedings of the IEEE/CVF Conference on Computer Vision and Pattern Recognition, Seattle, WA, USA, 13–19 June 2020; pp. 3636–3645.
34. Zhou, X.; Fang, H.; Liu, Z.; Zheng, B.; Sun, Y.; Zhang, J.; Yan, C. Dense Attention-guided Cascaded Network for Salient Object Detection of Strip Steel Surface Defects. *IEEE Trans. Instrum. Meas.* **2021**, *71*, 5004914. [[CrossRef](#)]
35. Zheng, B.; Yuan, S.; Yan, C.; Tian, X.; Zhang, J.; Sun, Y.; Liu, L.; Leonardis, A.; Slabaugh, G. Learning Frequency Domain Priors for Image Demoireing. *IEEE Trans. Pattern Anal. Mach. Intell.* **2021**. [[CrossRef](#)]
36. Zhao, H.; Zheng, B.; Yuan, S.; Zhang, H.; Yan, C.; Li, L.; Slabaugh, G. CBREN: Convolutional Neural Networks for Constant Bit Rate Video Quality Enhancement. *IEEE Trans. Circuits Syst. Video Technol.* **2021**. [[CrossRef](#)]
37. Zheng, B.; Tian, X.; Chen, Y.; Jiang, R.; Liu, X. Build receptive pyramid for efficient color image compression artifact reduction. *J. Electron. Imaging* **2020**, *29*, 033009. [[CrossRef](#)]
38. Zheng, B.; Sun, R.; Tian, X.; Chen, Y. S-Net: A scalable convolutional neural network for JPEG compression artifact reduction. *J. Electron. Imaging* **2018**, *27*, 1. [[CrossRef](#)]
39. Tian, X.; Zheng, B.; Li, S.; Yan, C.; Zhang, J.; Sun, Y.; Shen, T.; Xiao, M. Hard parameter sharing for compressing dense-connection-based image restoration network. *J. Electron. Imaging* **2021**, *30*, 053025. [[CrossRef](#)]
40. Lim, B.; Son, S.; Kim, H.; Nah, S.; Mu Lee, K. Enhanced deep residual networks for single image super-resolution. In Proceedings of the CVPRW, Honolulu, HI, USA, 21–26 July 2017.
41. Wang, X.; Yu, K.; Wu, S.; Gu, J.; Liu, Y.; Dong, C.; Qiao, Y.; Change Loy, C. Esrgan: Enhanced super-resolution generative adversarial networks. In Proceedings of the ECCV, Munich, Germany, 8–14 September 2018.
42. Kim, J.; Kwon Lee, J.; Mu Lee, K. Accurate image super-resolution using very deep convolutional networks. In Proceedings of the CVPR, Las Vegas, NV, USA, 27–30 June 2016.
43. Timofte, R.; Agustsson, E.; Gool, L.V.; Yang, M.H.; Zhang, L.; Lim, B.; Son, S.; Kim, H.; Nah, S.; Lee, K.M.; et al. NTIRE 2017 Challenge on Single Image Super-Resolution: Methods and Results. In Proceedings of the 2017 IEEE Conference on Computer Vision and Pattern Recognition Workshops (CVPRW), Honolulu, HI, USA, 21–26 July 2017. [[CrossRef](#)]
44. Bevilacqua, M.; Roumy, A.; Guillemot, C.; Alberi-Morel, M.L. Low-complexity single-image super-resolution based on nonnegative neighbor embedding. In Proceedings of the British Machine Vision Conference 2012, Surrey, UK, 3–7 September 2012; pp. 1–135.
45. Kingma, D.; Ba, J. Adam: A Method for Stochastic Optimization. In Proceedings of the ICLR, Banff, AB, Canada, 14–16 April 2014.
46. Yang, J.; Wright, J.; Huang, T.S.; Ma, Y. Image super-resolution via sparse representation. *IEEE Trans. Image Process.* **2010**, *19*, 2861–2873. [[CrossRef](#)] [[PubMed](#)]
47. Arbelaez, P.; Maire, M.; Fowlkes, C.; Malik, J. Contour detection and hierarchical image segmentation. *IEEE Trans. Pattern Anal. Mach. Intell.* **2010**, *33*, 898–916. [[CrossRef](#)] [[PubMed](#)]
48. Huang, J.B.; Singh, A.; Ahuja, N. Single image super-resolution from transformed self-exemplars. In Proceedings of the IEEE Conference on Computer Vision and Pattern Recognition, San Diego, CA, USA, 20–25 June 2005; pp. 5197–5206.
49. Matsui, Y.; Ito, K.; Aramaki, Y.; Fujimoto, A.; Ogawa, T.; Yamasaki, T.; Aizawa, K. Sketch-based manga retrieval using manga109 dataset. *Multimed. Tools Appl.* **2017**, *76*, 21811–21838. [[CrossRef](#)]
50. Dong, C.; Loy, C.C.; Tang, X. Accelerating the Super-Resolution Convolutional Neural Network. In Proceedings of the Computer Vision—ECCV 2016, Amsterdam, The Netherlands, 11–14 October 2016; Leibe, B., Matas, J., Sebe, N., Welling, M., Eds.; Springer International Publishing: Cham, Switzerland, 2016; pp. 391–407.

51. Wang, Z.; Bovik, A.; Sheikh, H.; Simoncelli, E. Image Quality Assessment: From Error Visibility to Structural Similarity. *IEEE Trans. Image Process.* **2004**, *13*, 600–612. [[CrossRef](#)]
52. Hui, Z.; Gao, X.; Yang, Y.; Wang, X. Lightweight image super-resolution with information multi-distillation network. In Proceedings of the 27th Acm International Conference on Multimedia, Nice, France, 21–25 October 2019; pp. 2024–2032.